


Amplification and regulation of periodic nanostructures in multipulse ultrashort laser-induced surface evolution by electromagnetic-hydrodynamic simulations

Anton Rudenko,^{*} Cyril Maclair, Florence Garrelie, Razvan Stoian, and Jean-Philippe Colombier[†]
Univ Lyon, UJM-St-Etienne, Laboratoire Hubert Curien, CNRS UMR 5516, F-42000, Saint-Etienne, France

 (Received 26 March 2019; revised manuscript received 24 May 2019; published 11 June 2019)

The formation of periodic structures in ultrafast laser-irradiated surfaces implies dynamic coupling between the incoming light and the light-driven material. To capture the mutual influence and feedback between light and evolving surface topographies, we investigate numerically the evolution of metal surfaces irradiated by multiple femtosecond laser pulses of sub-, near-, and slightly above-threshold ablation fluence. The multiphysical model combines Maxwell equations and thermohydrodynamic approach based on electron-ion heat transfer and compressible Navier-Stokes equations and allows us to account for interpulse feedback on the resulting surface topographies. First pulses of the subthreshold energy lead to material swelling, nanocavitation few tens of nanometers below the surface, and, as a result, nanoroughness formation on the initially flat surface. Further pulses contribute to the development of periodic surface structures, enhanced absorption, and increased removal rate. Cavitation in the tips of ripples is found to play a crucial role in modification and regulation of surface topography for sub- and near-threshold ablation fluences. At higher laser pulse energy, thermal ablation is mostly involved in surface modification, and the ablation rate per power reaches its maximum at three to five times the ablation threshold fluence, resulting from the optimal heat penetration depth for laser ablation. The numerical results offer a better understanding of the surface topography modifications upon multipulse femtosecond laser irradiation.

DOI: [10.1103/PhysRevB.99.235412](https://doi.org/10.1103/PhysRevB.99.235412)

I. INTRODUCTION

Ultrashort laser pulses with fluences below, near, and slightly above the ablation threshold open broad possibilities for precise and efficient fabrication of nano/microstructures on the surface of metals. These features can create, for example, unique antireflective, plasmonic, antibacterial, and wettability properties via single-pulse and multipulse irradiations [1–6]. The control over the topography aspect ratios, regularity, flexibility, and complexity of periodic and aperiodic laser-induced nanostructures still appears to be a complex issue owing to the fact that the surface relief is modified via numerous hydrodynamic phenomena, such as melt flow and capillarity effects [7,8], subsurface nanopallation [9], and ablative evaporation [10]. The nanoroughness induced by the evolution of the surface relief, in turn, influences the local energy deposition and temperature gradients from pulse to pulse [9,11,12]. Such dynamic coupling between incoming light and the light-driven material was recognized to give a positive feedback for periodic nanostructure ordering [12,13].

This way, multipulse laser irradiation of surfaces represents a nontrivial interplay between photothermal mechanisms of absorbed energy and heat confinement and hydrodynamic processes leading to phase transitions, melt flow, and material removal. For instance, laser interaction with subthreshold ablation fluence is characterized by material swelling [14–16],

formation of subsurface cavities [9,17], nanobumps, nanopillars, and nanojets above the initial surface level [1,4,18,19]. Multiple pulses were found to completely modify the surface relief producing significant roughness as well as periodic and aperiodic structures including ripples, spikes, and grooves [3,7,9,20]. Surface ablation by ultrashort laser pulses of higher energy results in void coalescence below the surface, spallation, thermal ablation, and phase explosion, creating an ablation crater, often surrounded by a crownlike rim [14,21,22]. Laser fluence was shown also to be a key parameter to define the ablation efficiency and the drilling processing quality, therefore the optimal laser irradiation regimes for industrial applications were intensively debated in the past few years [23–26].

Previously, hydrodynamic approaches have been developed to predict the ablation crater depth and to describe the plasma plume expansion in the regimes of ultrafast laser ablation [27–29]. Among them, one-dimensional hydrodynamic equations with incorporated equations of state (EOS) [30–32], molecular dynamics approaches [8,10,15,16,33,34], and incompressible hydrodynamic approaches based on Navier-Stokes equations [20,35,36] were applied to discuss the relative role of decomposition processes in laser ablation. An empirical model based on Kuramoto-Sivashinsky was implemented by Reif *et al.* [37] in order to discuss the processes of nanostructure self-organization. Describing the particular type of instability caused by surface erosion and atomic diffusion, the model is not adequate to relate accurately the laser irradiation conditions to surface modifications. A three-dimensional hydrodynamic approach based on

^{*}antmipt@gmail.com

[†]jean.philippe.colombier@univ-st-etienne.fr

incompressible Navier-Stokes equations coupled with a two-temperature model was proposed by Tsibidis and co-workers [7,20]. On one side, with the terms of viscosity and surface tension, the capillarity effects have been taken into account in this approach, and the formation mechanism of suprawavelength structures on semiconductors, dielectrics, and metals was explained in terms of convection rolls and hydrothermal waves established pulse by pulse [7]. On the other side, the model does not describe the compressible photomechanical processes, such as subsurface nanocavitation and spallation, which can strongly influence the hydrodynamics and pulse-to-pulse evolution. Additionally, if several pulses are considered, Maxwell equations should be solved in order to define accurately the energy deposition on the new surface relief. For instance, the electromagnetic approaches underlined the crucial role of coherent scattering on surface nanoroughness in ripple formation [9,11,12,38,39]. The absorption distributions on rough surfaces calculated by full-vector Maxwell equations were investigated by Skolski *et al.* [39], revealing similarities in orientation and periodicity between these patterns and ripples observed in experiments. The model was further expanded to account for positive interpulse feedback [39], transient electronic properties [11], thermal diffusion, and ablation [12]. However, these approaches have never been coupled to a full system of hydrodynamic equations to describe the transition from electromagnetic or electron-density patterns to permanent modifications and to elucidate the role of multipulse feedback.

We propose a multiphysical approach to describe accurately the evolution of the surface relief at below- and near-ablation femtosecond irradiation conditions. First, Maxwell equations are solved to define the energy absorption distribution on the metal surface. The incorporation of Maxwell equations into the multipulse laser ablation model allows us to consider the consequences of light interference with both radiative and nonradiative scattered fields from nanostructures, such as nanoholes or nanobumps [40]. The numerical solutions account for both evanescent surface waves and their plasmonic counterparts [12]. This way, the multiphysical model allows us to follow the surface evolution through the stages of disorder, self-organization, amplification, and regulation of the laser-induced nanostructures. Then, the electron heat transfer equations are coupled with compressible Navier-Stokes equations with incorporated equations of state and viscosity terms to define temperature and lattice density distributions after fluid movement, material decomposition, and removal. The proposed model combines the variety of physical phenomena, previously discussed only separately within compressible [30,31] and incompressible [7,20] hydrodynamic and electromagnetic [11,39] approaches. Within the described approach, we show different multipulse pathways of surface relief evolution provided by ultrashort laser irradiation. In contrast to previous electromagnetic models [11,12,39], we start from the initially flat surface, therefore, the surface topography evolution is dictated solely by laser irradiation conditions. Mechanisms of roughness and ripple formation, amplification, and regulation on the surface and in the ablation crater are elucidated, and the optimal laser irradiation strategies for efficient ablation are proposed.

II. NUMERICAL MODEL

A. Energy deposition

The absorbed energy is calculated based on the solution of Maxwell equations,

$$\begin{aligned}\frac{\partial \vec{E}}{\partial t} &= \frac{\nabla \times \vec{H}}{\epsilon_0} - \frac{1}{\epsilon_0} \vec{J}, \\ \frac{\partial \vec{H}}{\partial t} &= -\frac{\nabla \times \vec{E}}{\mu_0},\end{aligned}\quad (1)$$

where \vec{E} is the electric field, \vec{H} is the magnetic field, ϵ_0 and μ_0 are free space permittivity and permeability, and \vec{J} is the electric current derived from the Drude model for the dispersive media by using the finite-difference time-domain (FDTD) method via the auxiliary differential equation method [41] as follows:

$$\frac{\partial \vec{J}}{\partial t} + \vec{J}/\nu = \epsilon_0 \omega_{pl}^2 \vec{E}, \quad (2)$$

where ω_{pl} is the plasma frequency and ν is the collision frequency. The effective values for the collision frequency and for the plasma frequency are deduced from the Drude formula approximation for real and imaginary parts of permittivity and the known refractive indices n and k as $\nu = 2nk\omega/(1 - n^2 + k^2)$ and $\omega_{pl}^2 = (\omega^2 + \nu^2)(1 - n^2 + k^2)$, where $\omega = 2\pi c/\lambda$ is the laser frequency and the laser wavelength is fixed to be $\lambda = 800$ nm. The refractive indices for excited stainless steel are evaluated as a function of the electron temperature based on the results of *ab initio* calculations for stainless steel [42]. At the edges of the grid, absorbing boundary conditions related to convolutional perfect matched layers are set to avoid nonphysical reflections [43]. The absorbed energy is defined as $I\alpha_{abs}$, where $I = \frac{n}{2} \sqrt{\frac{\epsilon_0}{\mu_0}} |\vec{E}|^2$ is the intensity and α_{abs} is the bremsstrahlung absorption coefficient related to the extinction coefficient k as $\alpha_{abs} = 4\pi k/\lambda$ [40].

A femtosecond Gaussian pulse in space and time is introduced as the linear-polarized electric-field excitation source focused in the center of the grid ($x = 0$, $z = 0$) with central wavelength $\lambda = 800$ nm,

$$\begin{aligned}E_x(t, x, z) &= \frac{w_0}{w(z)} \exp\left[-\frac{(t - t_0)^2}{\tau^2}\right] \\ &\times \exp\left[-\frac{x^2}{w(z)^2} - 2i\pi z/\lambda - \frac{i\pi x^2}{R(z)\lambda} + i\zeta(z)\right],\end{aligned}\quad (3)$$

where $\tau = 80$ fs is the pulse width at half maximum, $t = t_0 = 160$ fs corresponds to the pulse energy maximum, $w_0 = 5 \mu\text{m}$ is the beam-waist radius, $w(z) = w_0 \sqrt{1 + (\frac{z}{z_R})^2}$ is Gaussian's beam spot size, $z_R = \pi w_0^2/\lambda$ is the Rayleigh length, $R(z) = z[1 + (\frac{z_R}{z})^2]$ is the radius of curvature of the beam's wave front, and $\zeta(z) = \arctan(\frac{z}{z_R})$ is the Gouy phase shift. Light propagates downwards along the $0z$ axis, whereas the light polarization is along the $0x$ axis.

B. Electron-ion heat transfer equations

Electron and ion temperatures are calculated in the frames of the two-temperature model (TTM) [27,44,45] where the energy conservation law is written as follows:

$$C_e \frac{\partial T_e}{\partial t} = \nabla \cdot (k_e \nabla T_e) - \gamma_{ei}(T_e - T_i) + I\alpha_{abs}, \quad (4)$$

$$\rho C_i \left[\frac{\partial T_i}{\partial t} + \vec{u} \cdot \nabla T_i \right] = \nabla \cdot (k_i \nabla T_i) + \gamma_{ei}(T_e - T_i),$$

where γ_{ei} is the electron-lattice coupling factor, C_e and C_i are the electron and the lattice heat capacities, respectively, ρ is the material density, k_e and k_i are the electron and the lattice thermal conductivities, \vec{u} is the displacement velocity, and $\vec{u} \cdot \nabla T_i$ is the convection term.

Electron temperature dependencies of nonequilibrium thermodynamic properties, such as $C_e(T_e)$, $k_e(T_e)$, and $\gamma_{ei}(T_e)$ as well as the electronic pressure $P_e(T_e)$ are taken from the results of *ab initio* calculations for stainless steel [42]. $C_i(T_i, \rho)$ is defined by the EOS [46] and accounts for phase transitions. The lattice thermal conductivity $k_i(T_i)$ for the solid state is adopted from Refs. [47,48]. Special convection boundary conditions for T_e and T_i are introduced on the interface as well as the insulated boundary conditions at the borders of the grid. The initial temperatures are set to be 300 K.

C. Hydrodynamic equations

To model the hydrodynamic evolution of the material density, we solve compressible Navier-Stokes equations in Eulerian form [49]. Momentum conservation for fluid flow [50] is written as follows:

$$\begin{aligned} \frac{\partial(\rho \vec{u})}{\partial t} + (\vec{u} \cdot \nabla)(\rho \vec{u}) + (\rho \vec{u}) \nabla \cdot \vec{u} \\ = -\nabla P + \mu \nabla^2 \vec{u} + \frac{1}{3} \mu \nabla(\nabla \cdot \vec{u}), \end{aligned} \quad (5)$$

where $\mu(T_i)$ is the temperature-dependent dynamic viscosity taken from Ref. [47] and P is the pressure, taking account both for electronic P_e and for ionic P_i contributions defined by EOS [46] $P = P_{EOS}(T_i) + P_e(T_e) - P_e(T_i)$ [30]. The sponge absorbing boundary conditions are introduced for displacement vectors \vec{u} [51,52].

The system of Navier-Stokes equations is completed by the mass conservation law,

$$\frac{\partial(\rho V)}{\partial t} + \nabla \cdot (\rho V \vec{u}) = 0, \quad (6)$$

where $0 \leq V \leq 1$ is the fractional volume open to flow, $V = 0$ corresponds to cells free from the fluid (vacuum), $V = 1$ corresponds to compressible fluid totally occupying the mesh, and $0 < V < 1$ for the interface cells. The described system of equations conserves energy, momentum, mass, and treats accurately the fluid flow via the introduction of volume-of-fluid (VOF) technique applied for the interface cells [53,54].

Figure 1 shows the typical laser-induced phase transitions which occur during ultrashort laser interaction with metal targets. The solid state is described by a system of equations for compressible fluid (4)–(6) with infinitely high viscosity.

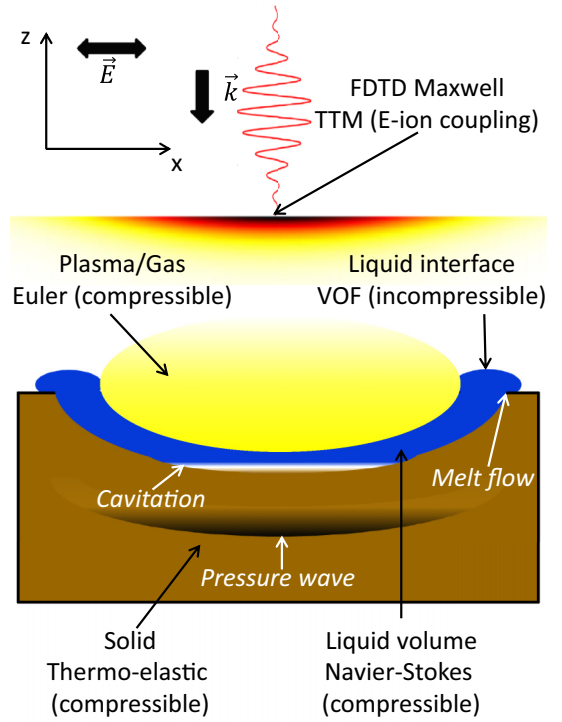


FIG. 1. Schematics of the considered multiphysical model where the following approaches are combined: Maxwell equations solved by the FDTD method, electron-ion heat transfer and diffusion equations solved by the TTM, and Navier-Stokes equations in Eulerian form using the VOF technique. Involved hydrodynamic processes and phase transitions under femtosecond laser irradiation are indicated.

Density dynamics supported by EOS-defined pressures allows us to model shock and rarefaction wave propagation in a solid. A liquid state is divided on the intrinsic part where the full compressible Navier-Stokes equations are evaluated and the interface part where the VOF method is applied. Such subdivision is crucial to consider both compressible phenomena, such as mechanically induced cavitation in liquid, and incompressible phenomena, such as melt flow due to Marangoni and recoil pressure forces. According to mass conservation law (6), $\sum_i \rho_i V_i = \text{const}$ in the entire volume, where ρ_i is the lattice density and V_i is the volume fraction in the considered cell. In the compressible part of the model, the volume fraction is kept constant, whereas the lattice density is modified via $\partial \rho / \partial t + \nabla \cdot (\rho \vec{u}) = 0$. For the incompressible part, VOF is applied where the density is kept constant and equal to the density in the neighbor volume cell, but the volume fraction at the interface is calculated by $\partial V / \partial t + \nabla \cdot (V \vec{u}) = 0$. The following transitions between these two parts are implied. If a neighbor cell is filled with $V = 1$, then the interface cells of the filled cell are treated with the changeable volume fraction but fixed density, and the filled cell becomes intrinsic and treated in a compressible way with $V = 1$ and changeable density via continuity equation (6). In contrast, if the cell is empty, $V = 0$, and the neighbor cells become interface cells with changeable volume fraction. The gas and plasma are treated by the Eulerian form of Navier-Stokes equations with zero viscosity and thermal conductivity. This way, the material

removal via the ablation process is fulfilled in the model by EOS pressure-driven mass transfer.

Cavitation in liquid or subsurface void formation is supported by the probabilistic Grady criterion [9,31,55], indicating that the local decomposition takes place if the negative pressures $P_i < 0$ are held during time $t > 6c\rho\gamma/P_i^2$, where $\gamma = \gamma_0(1 - T_i/T_{cr})^{1.25}$ is the temperature-dependent surface tension $\gamma_0 = 1.872$ N/m [48], $c = 3.2$ km/s is the speed of sound in liquid stainless steel, and $T_{cr} = 8582$ K is the critical temperature for stainless steel [46].

D. Calculation details

We use a fixed mesh with spatial steps $\Delta z = 1$ nm along the propagation direction and $\Delta x = 10$ nm along the laser polarization. The grid mesh is composed of 2000×2000 cells, which corresponds to the dimensions of $2 \times 20 \mu\text{m}^2$. The higher resolution in the $0z$ direction is necessary to model accurately the light absorption on a metal surface. A changeable temporal step is used in our simulations, depending on the relevant physical processes occurring on different timescales. The procedure is similar to the one applied for laser interaction with transparent materials, previously described in Ref. [56]. The smallest temporal step of ≈ 1.5 as is used whereas solving Maxwell equations during laser pulse propagation. It is increased after the pulse up to the optical cycle ≈ 2.7 fs and maintained constant during electron-ion thermal transfer and electron-gas cooling. Then, the temporal step is once again increased up to ≈ 15 fs. Surface modifications occurring up to the 100-ps scale as well as pressure wave propagation are calculated with this time step.

III. RESULTS AND DISCUSSION

A. Subsurface cavitation

The material decomposition in the laser-affected zone commonly occurs following thermal or mechanical scenarios [31,33]. The ablation threshold, typically in the range of $F \approx 0.09\text{--}0.21$ J/cm² for stainless steel [24,57–59], indicates often the initiation of classical thermal ablation when referring to evaporation of the solid material into the ablation plasma. In the case of ultrashort laser irradiation by a subthreshold fluence, the modification may occur below the metal surface as a consequence of a strong rarefaction wave, following the pressure wave induced by thermal gradients [8,15,16].

We start our investigation by analyzing single-pulse evolution of an initially flat surface. We focus on pressure wave propagation and density changes in the surface and below the surface. These effects occur as soon as the lattice temperature gradients are established after the electron-ion thermal transfer. The characteristic time for electron-gas cooling due to energy exchange with lattice is defined by the ratio of electron heat capacity and electron-ion coupling factor [29], which is $C_e/\gamma_{ei} > 1$ ps for stainless steel. The maximum temperatures corresponding to the considered fluence $F = 0.15$ J/cm² do not exceed the boiling temperatures $T \approx 3145$ K, however, the thin surface layer is melted. Material density snapshots shown in Fig. 2 reveal the propagation of the pressure wave at first tens of picoseconds with the speed approaching the

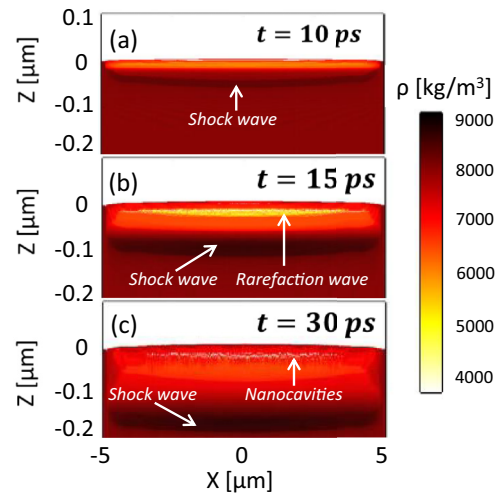


FIG. 2. Lattice density snapshots upon single-pulse ultrashort laser irradiation with peak fluence $F = 0.15$ J/cm² at different time delays on stainless steel. The time after the material excitation t is indicated in each figure.

speed of sound in solid stainless steel $c = 5.8$ km/s. The densification wave is accompanied by the rarefaction wave launched to the opposite direction. The rarefaction is characterized by strong negative pressures, evaluated by the equation of state. Cavities of nanometric sizes are formed several tens of nanometers below the surface where the Grady criterion for mechanical decomposition is satisfied [55]. As a consequence, the fluid is pushed to the level well above the initial one. The material expansion takes place up to tens of picoseconds.

B. Multipulse dynamics

To elucidate the multipulse evolution of the laser-affected zone, we assume that surface relief is modified within the considered timescale of ≈ 100 ps. Lattice cooling is achieved on the scale of thermal diffusion time on the order of few microseconds [60]. We thus neglect heat accumulation effects assuming that the time between successive pulses is above the microsecond (i.e., pulse repetition rate below the megahertz regime). At the beginning of each new pulse, we set both electron and material temperatures equal to 300 K. The diffusion limit time can be estimated as $w_0^2/D \approx 4.2 \mu\text{s}$ for stainless steel, where $w_0 = 5 \mu\text{m}$ is the laser spot radius and $D \approx 6 \times 10^{-6}$ m²/s is the thermal diffusivity. Experimentally, the excessive heat accumulation effects result in the growth of microscale roughness and uncontrollable degradation of surface profile [61,62]. For stainless steel, the ablation regimes with repetition rates up to 500–600 kHz, and fluences up to ten times the ablation threshold were reported to conserve good machining quality upon multipulse femtosecond laser irradiation. One can relate this to the absence of significant heat accumulation. We also do not consider the effects of plasma shielding, nanoparticle generation in the laser-induced plasma plume, and redeposition of the ablation species on the surface, which influence the laser ablation in the case of high repetition rates or extremely high fluences, more than ten times exceeding the ablation threshold [24,62–64]. We also neglect the

influence of background gas or air on plasma plume evolution during laser ablation, considering the background medium as a vacuum. We consider the results for shallow ablation depths, although similar calculations can be performed for deeper ablation depths, for instance, see Ref. [12], where full-vector Maxwell equations take account for reflections from the borders of the ablation crater. The physical limitation of the model in this case is related to fluences strongly exceeding the ablation threshold. For these laser irradiation conditions, the laser-induced plasma and slowly moving nanoparticles are generated, preventing the evacuation of the ablated material before the next pulse arrives. This effect is non-negligible for deep holes and would require the development of more advanced models.

Starting from the initially flat surface, we take account both for surface relief modification and intrinsic changes, including subsurface cavity formation. The next pulse calculations redefine the absorbed energy deposition by solving Maxwell equations (1) and (2), and Eqs. (4)–(6) are solved for the new surface relief. As a result, we present the electromagnetic snapshots representing the energy deposition on the modified surface and the surface topography at the same time.

1. Subthreshold fluence

Figures 3(a)–3(d) show the evolution of the surface morphology during irradiation by multipulse subthreshold ultrashort laser pulses. For the first few laser pulses, the energy is not enough to ablate thermally the surface. We note, however, the formation of nanocavities below the surface and expansion

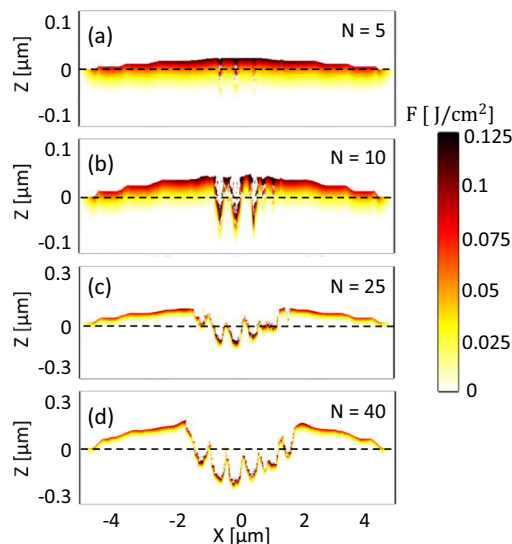


FIG. 3. Energy deposition after multipulse ultrashort laser irradiation with peak fluence $F = 0.125 \text{ J/cm}^2$ on stainless steel. Here and further, every image with the number of pulses N corresponds to the absorbed energy during the N th pulse after pulse propagation but before surface modification. The initial surface level is marked by the dashed black line. The evolution of surface topography consists of (a) subsurface nanocavitation and swelling, (b) roughness amplification, and (c) and (d) formation of a volcanolike ablation crater covered with ripples.

of the surface well above the initial level in Fig. 3(a). Material swelling and subsurface nanovoids below the surface as a first step of laser ablation of metals were previously observed [9,14,17] and investigated within the molecular dynamics approach [15,16]. From pulse to pulse, the electromagnetic field is more and more reinforced in a thin nanometric surface layer due to the presence of the laser-induced nanovoids. The enhancement around the nanovoids is mainly due to the cavitation process that takes place below the surface at distances comparable to light absorption depth. This way, surface waves can be still excited by inhomogeneities, resulting in localization of the absorption energy in vicinity of the nanocavity. As a result, higher temperatures and larger probabilities of spall are achieved. This way, the voids become larger until the energy is enough to open the voids and form a nanohole on the surface. The numerical results demonstrate that tens of pulses are required to achieve the significant enhancement for ablating holes of 100-nm size in Fig. 3(b). The electromagnetic field is now localized at the bottom of the holes and promotes the growth and the expansion of the ablated zone by thermal ablation. The sequence of 40 pulses indicates that the final modification represents a volcanolike crater of a few hundred nanometers covered with ripples in Fig. 3(d). The material expansion above the initial surface in this case is entirely the consequence of subsurface nanovoid formation and mass conservation. The ripple periodicity is close to the laser wavelength, and their appearance is directly related to the interference of the incident light with the radiative scattered fields from laser-induced inhomogeneities [9,12,39]. Ripple periods on metal surfaces decrease with the number of applied pulses, therefore, different values were reported depending on laser irradiation conditions [65]. Upon multipulse irradiation, however, the regulation of periods occurs where the contrast between maximum and minimum periods decreases [66]. Furthermore, the periods saturate and do not evolve anymore upon multipulse irradiation. The evolution from random surfaces to well-ordered ripples by multipulse ablation was discussed in Ref. [12] where the saturation value of $\approx 3\lambda/4$ was theoretically explained. In our case, it is shown that the periodic structures are formed by irradiation of a perfectly flat surface, whereas the roughness is the consequence of hydrodynamic processes of material decomposition. Here and further, low-spatial frequency periodic surface structures are obtained by two-dimensional multipulse simulations. The formation of the nanostructures with smaller periodicities is out of the scope of the present article, requiring three dimensionality [40], and the high-spatial frequency ripple emergence and evolution will be reported elsewhere. The limitation comes from the fact that two-dimensional Maxwell equations do not account for polarization-dependent nonradiative response on the plane perpendicular to the propagation plane. They also do not consider the finite size of the nanostructures on this plane, dealing with infinite gratings rather than periodic holes. Slight differences are expected in thermal diffusion, shock wave, and rarefaction wave propagation as well as the dimensions of subsurface cavities and rim above the surface level. Nevertheless, the two-dimensional results still provide a realistic picture of the phenomena, occurring during femtosecond laser-matter interactions and inaccessible by one-dimensional approaches.

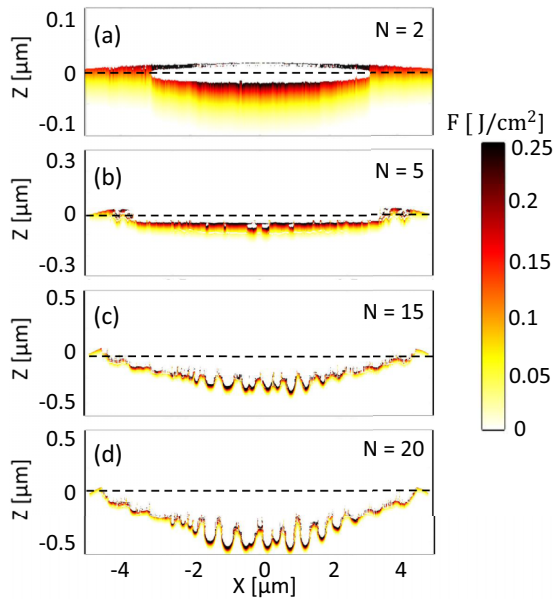


FIG. 4. Energy deposition after multipulse ultrashort laser irradiation with peak fluence $F = 0.25 \text{ J/cm}^2$ on stainless steel. The number of pulses N is indicated on each figure. The initial surface level is marked by the dashed black line. Surface topography images show the evolution of the modification through (a) spallative ablation, (b) roughness amplification, and (c) and (d) ripple formation in the ablated crater.

2. Near-threshold fluence

If the peak fluence is increased up to $F = 0.25 \text{ J/cm}^2$, the effect of the pressure wave leads to mechanical ablation or spallation. An elongated cavity of several micrometers is formed below the surface as a result of nanovoid coalescence as shown in Fig. 4(a). Further ablation leads to the void opening and spallation of several tens of nanometers at one pulse in Fig. 4(b). Significant roughness is formed in the ablation crater after spallation and material removal. The electromagnetic-field enhancement in the holes promotes the growth of ripples up to $H \approx 200\text{-nm}$ depth after 20 pulses irradiation as shown in Fig. 4(d). The limitation for their growth is not related directly to thermal ablation of the peaks but to formation of nanoscale cavities inside the ripple tips, consequent field enhancement, and then partial material removal. Note that the temperatures are not enough to ablate the peaks thermally if the nanocavities are not induced by previous pulses. The stabilized ripple periodicity is slightly smaller than the laser wavelength ($\approx 3\lambda/4$), which is the consequence of topography-mediated electromagnetic feedback, previously discussed in Ref. [12].

3. Above-threshold fluence

Series of calculations are performed also for peak fluence above the ablation threshold $F = 0.5 \text{ J/cm}^2$ for stainless steel shown in Figs. 5(a)–5(c). The maximum temperatures attained by single-pulse irradiation exceed the boiling point in this case. The ablation depth is given mostly by the temperature distribution. A sequence of 10–20 pulses results in ripple formation with periodicity $\approx 3\lambda/4$, however, the laser-induced

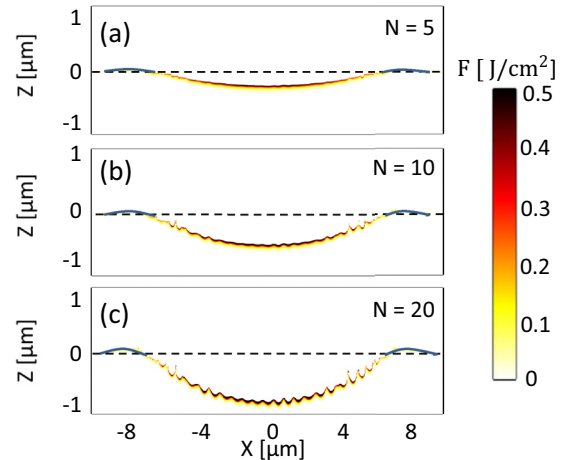


FIG. 5. Energy deposition after multipulse ultrashort laser irradiation with peak fluence $F = 0.5 \text{ J/cm}^2$ on stainless steel. The number of pulses N is indicated on each figure. The initial surface level is marked by the dashed black line. Surface topography images evidence the appearance of ablation crater covered with ripples and surrounded by a thin rim above the initial surface level marked by solid blue line.

temperatures are now sufficient to remove the material both in the bump crests and in the holes. This way, the growth of periodic surface structures is limited by $H \approx 200 \text{ nm}$. The quality of the ablated crater is improved in terms of ablation depth to average roughness ratio. The snapshots of the surface relief shown in Figs. 5(a)–5(c) indicate the presence of a 100-nm rim above the initial surface level, created due to fluid flow of liquid material over the solid one outside the laser-affected zone. In contrast to the case of subthreshold fluences and volcanolike crater shown in Fig. 3, the material movement here is governed by thermal ablation liquid flow at the borders of the crater. The rim height is shown to increase with fluence. For instance, for a fixed number of applied pulses $N = 20$, the rim height $H \approx 75 \text{ nm}$ for fluence $F = 0.25 \text{ J/cm}^2$ in Fig. 4(d) and $H \approx 150 \text{ nm}$ for fluence $F = 0.5 \text{ J/cm}^2$ in Fig. 5(c). Additionally, the rim grows from $H \approx 100 \text{ nm}$ in Fig. 5(b) to $H \approx 150 \text{ nm}$ in Fig. 5(c) with the increasing number of applied pulses.

4. Amplification and regulation of ripple profile

Multipulse dynamics of surface topography is driven by the interplay of electromagnetic and hydrodynamic processes, that interchangeably play constructive and destructive roles. For instance, the formation of subsurface voids increases the absorption on the rough surface. The energy absorption below the holes and ripple hollows results in the profile deepening and the roughness amplification. Therefore, ripples, once formed, are not erased but only become more pronounced by electromagnetic effects and pulse-by-pulse material removal. Figure 6(a) shows, however, that the growth is limited to $\approx 200\text{-nm}$ depths if fluences near the ablation threshold are applied. The reason for such regulation is purely hydrodynamic. The density distribution 50 ps after irradiation by the third laser pulse is plotted in Fig. 6(b). The material is removed below ripple hollows, whereas the liquid layer is formed at

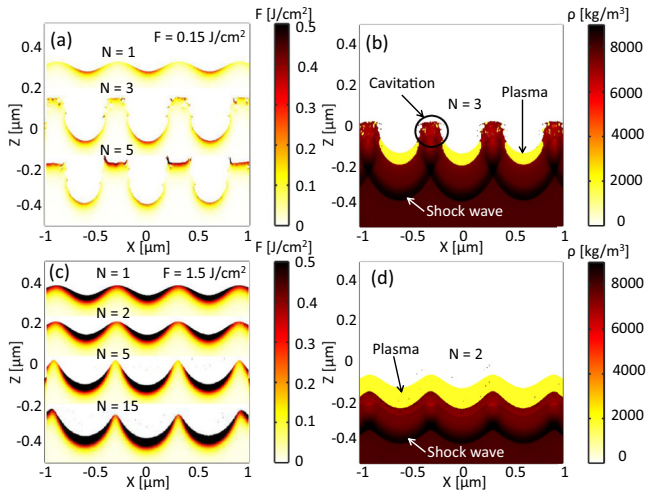


FIG. 6. Evolution of ripple topography with periodicity $\lambda = 600$ nm by multipulse irradiation of ultrashort laser pulses with (a) $F = 0.15$ J/cm² and (c) $F = 1.5$ J/cm². Density snapshots 50 ps after irradiation (b) by $F = 0.15$ J/cm² and $N = 3$, (d) by $F = 1.5$ J/cm² and $N = 2$. Surface topography images indicate nanostructure amplification and regulation via (a) cavitation in the tips for lower fluence and (c) electromagnetic feedback for higher fluence.

the tips where the energy is not enough to start the ablation process. Such configuration results in rarefaction wave confinement inside the nanostructure and high probability of mechanically induced cavitation. As the nanocavities are formed inside the ripple crests, the electric field is now enhanced around the nanovoids, and the energy is enough to ablate the tips. The ripple shape turns to be flatter, therefore, the energy is absorbed both in hollows and in crests in Fig. 6(a) for $N = 5$ pulses, which does not allow the nanostructures to grow deeper.

A different mechanism is predicted by numerical simulations for higher fluences above the ablation threshold. As the ripples become deeper, the absorption increases, resulting in higher volumes of removed material by thermal ablation in Fig. 6(d). Following the ripple profile evolution upon $N = 15$ pulses irradiation in Fig. 6(c), one can note that the shape of the nanostructures changes from regular sinusoidal to sinusoidal with triangular stretched tips. On such a modified profile, the energy is still absorbed stronger below the holes than at the peaks of the nanostructures. However, the peaks are narrow, as a result of multipulse laser ablation. Due to excessive thermal diffusion, these regions, having dimensions smaller than heat penetration depth, gain high temperatures and are removed by the following pulse. The regulation of ripple depth and uniform distribution of lattice densities along the surface profile shown in Fig. 6(d) is the consequence of this effect.

Although the results are shown for ripple profiles of a fixed periodicity $\lambda = 600$ nm for which the spatial pattern stability is already achieved [12], both of the described regulation mechanisms take place for any subwavelength periodic or quasiperiodic profiles, including high-spatial frequency ripples. However, if the characteristic spacings exceed the laser wavelength, as in the case of spikes or grooves, the absorbed

energy is distributed equally all along the profile, and the ablation does not lead to the microstructure amplification or erasure.

C. Efficiency vs quality

The numerical results indicate that the laser irradiation with fluence slightly above the ablation threshold gives cleaner ablation crater than the irradiation with subthreshold and near-threshold ablation. Furthermore, the laser energy dose defined as laser fluence multiplied by the number of applied pulses is an important parameter in order to define the efficiency of ultrashort laser ablation. The ablation depth or the volume of the ablated material does not scale linearly with laser fluence [44,45], therefore, there is an optimal value of fluence corresponding to the minimum laser energy dose required to drill the hole of desirable depth or more efficient ablation. The efficiency in this case relies on the fact that the thermally affected zone scales nonlinearly with laser fluence. If we increase the laser fluence twice, the thermal diffusion depth increases less than twice, which makes thermal ablation inefficient at fluences several times exceeding the ablation threshold [23,26]. We perform numerical simulations in order to elucidate this trend.

Figure 7 shows the temperature profiles after irradiation by multiple pulses of equal laser energy dose $5 \mu\text{J}$ but different fluence and number of applied pulses. The temperatures are limited by the boiling temperature for stainless steel $T_{\text{boil}} = 3145$ K, therefore, the black color stands for the amount of material which is expected to be removed by the next pulse. The ablation depth per pulse, comprising or not including the roughness, as well as the ablation depth per fluence are plotted as a function of laser fluence in Fig. 7(e).

The regimes of subthreshold pulses show poor efficiency and surface quality in Fig. 7(a). The surface profile is degraded both due to multipulse expansion in accumulative regime and inhomogeneous low-energy deposition below the laser-induced nanoholes. The ablation depth increases rapidly up to few hundred of nanometers if the higher fluences close to the ablation threshold are considered as in Fig. 7(b). In this regime, the material removal is both due to spallation as the initial step of ablation and to thermal ablation amplified by the laser-induced surface roughness. Thermal penetration depth per fluence has not reached its maximum, however, the value increases due to ripple formation and the large amount of nanometric holes. The ablation crater formed by $F = 0.2\text{--}0.3$ J/cm² irradiation is characterized by the highest ratio between the laser ablation depth and roughness contrast for a fixed laser energy dose, which is seen from the dotted black curve plotted in Fig. 7(e). In contrast, surface roughness generated by ultrashort laser ablation with fluences close and two to three times exceeding the ablation threshold is amplified pulse by pulse, reaching 100 nm, but is not sensitive to the exact value of the laser fluence. A similar observation was also performed in Ref. [66]. Furthermore, the maximum ablation depth with fixed total amount of energy is achieved whereas irradiating by laser pulses with fluence three times exceeding the ablation threshold $F \approx 0.4\text{--}0.5$ J/cm² in Fig. 7(e). The multipulse evolution of the surface profile under such fluence was demonstrated in Fig. 5. A further increase in fluence does

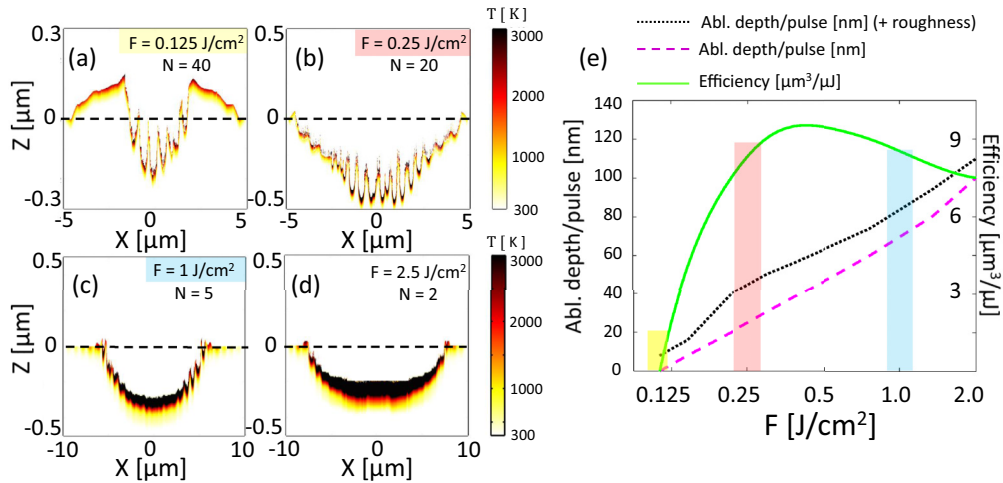


FIG. 7. (a)–(d) Temperature distributions after multipulse ultrashort laser irradiation with an equivalent laser energy dose and varying fluences and number of applied pulses (a) $F = 0.125 \text{ J/cm}^2$, $N = 40$; (b) $F = 0.25 \text{ J/cm}^2$, $N = 20$; (c) $F = 1.0 \text{ J/cm}^2$, $N = 5$; (d) $F = 2.5 \text{ J/cm}^2$, $N = 2$ on stainless steel. Every image with the number of pulses N corresponds to the maximum temperature distribution after the N th pulse propagation and electron-ion thermal equilibrium but before surface modification. The initial surface level is marked by a dashed black line. (e) Ablation depth per pulse, including (dotted black curve) and excluding (dashed magenta curve) surface roughness and ablation efficiency dependence on laser fluence. The values corresponding to (a)–(c) regimes are colored by yellow, red, and blue correspondingly.

not show better performance, for example, if one compares the ablation depth in Fig. 7(c) and in Fig. 7(d) for the corresponding fluences $F = 1$ and $F = 2.5 \text{ J/cm}^2$. The thermal penetration depth increases with laser fluence but slower than the applied fluence. Note that roughness is negligible in both cases of above-threshold ablation but mostly because of lower number of required pulses $N \leq 5$. Irradiation by a higher number of pulses will result in ripple formation in the ablation crater as discussed in Ref. [12].

The ablation depths per pulse measured without taking account for roughness calculated by multipulse simulations and shown in Fig. 7(e) quantitatively agree with the experimental measurements of typical ablation depths per pulse for gentle and strong femtosecond laser ablation phases. For example, one finds 30–40-nm ablation depths for $F = 0.5 \text{ J/cm}^2$ and 80–90-nm ablation depths for $F = 2 \text{ J/cm}^2$ reported in Refs. [22,57,67].

We propose that the presented results explain the existence of an optimal laser fluence slightly exceeding the ablation threshold, reported previously in the case of laser ablation of different metals, including stainless steel [23,26]. In fact, the heat penetration depth can be estimated as $x = \sqrt{\frac{128}{\pi}} \left(\frac{K_e^2 T_e C_{i\rho}}{T_m \gamma_{ei}^2 C_e} \right)^{1/4}$ [44], where T_m is the material melting temperature. Taking into account the almost linear dependence of $K_e \propto T_e$ and $C_e \propto T_e$ on the electron temperature [42,68], one can derive $x \propto \sqrt{T_e / \gamma_{ei}}$. For most of the materials, such as stainless steel or nickel, the electron-ion coupling factor γ_{ei} either decreases slower than $\gamma_{ei} \propto T_e^{-1}$ for $T > 10 \text{ kK}$ or increases as in the case of aluminum, silver, or gold [42,68]. Such a behavior results in a weaker than linear growth of heat penetration depth or the ablation depth as a function of the electron temperature or the laser fluence. As a consequence, the ablation efficiency starts to decrease from a certain pulse energy above the ablation threshold. Further investigations are required to verify if the similar trends are common for other

metals. The efficiency of laser drilling can be further improved by benefiting from heat accumulation if the high repetition rates are used or by consequent double-pulse or multiple-pulse burst irradiation [24]. In this case, the effective fluence per pulse would increase, the regimes of above-threshold ablation are expected to be achieved within the superposition of subthreshold pulse trains. This study is out of the scope of our investigation.

IV. GENERAL ABLATION TRENDS

General trends in femtosecond laser-induced ablation of metal surfaces revealed by coupled electromagnetic and hydrodynamic calculations are summarized in Fig. 8, classified by required laser fluence and number of applied pulses. The first pulse results in subsurface cavitation on the nanoscale, formation of a microvoid below the surface, or thermal ablation depending on laser fluence. The corresponding lattice density snapshots are illustrated at the bottom of Fig. 8. The typical optical response of the deformed surfaces are then demonstrated in the upper row corresponding to the second pulse irradiation. Among them, local field enhancement by created subsurface voids is underlined. The next upper row details the typical surface profile irradiated by several pulses, consisting of surface nanoroughness and ripples. Then, the mechanisms of periodic structure regulation are detailed in the upper part of Fig. 8. For near-threshold fluences, the hydrodynamic scenario is expected where the cavitation takes place in the melted tips of the nanostructures, which are further removed by the following pulses due to strong local field enhancement on subsurface nanovoids. For higher fluences, the electromagnetic feedback dominates over the hydrodynamic processes, resulting in shape modification of ripples and homogeneous thermal diffusion on the whole surface.

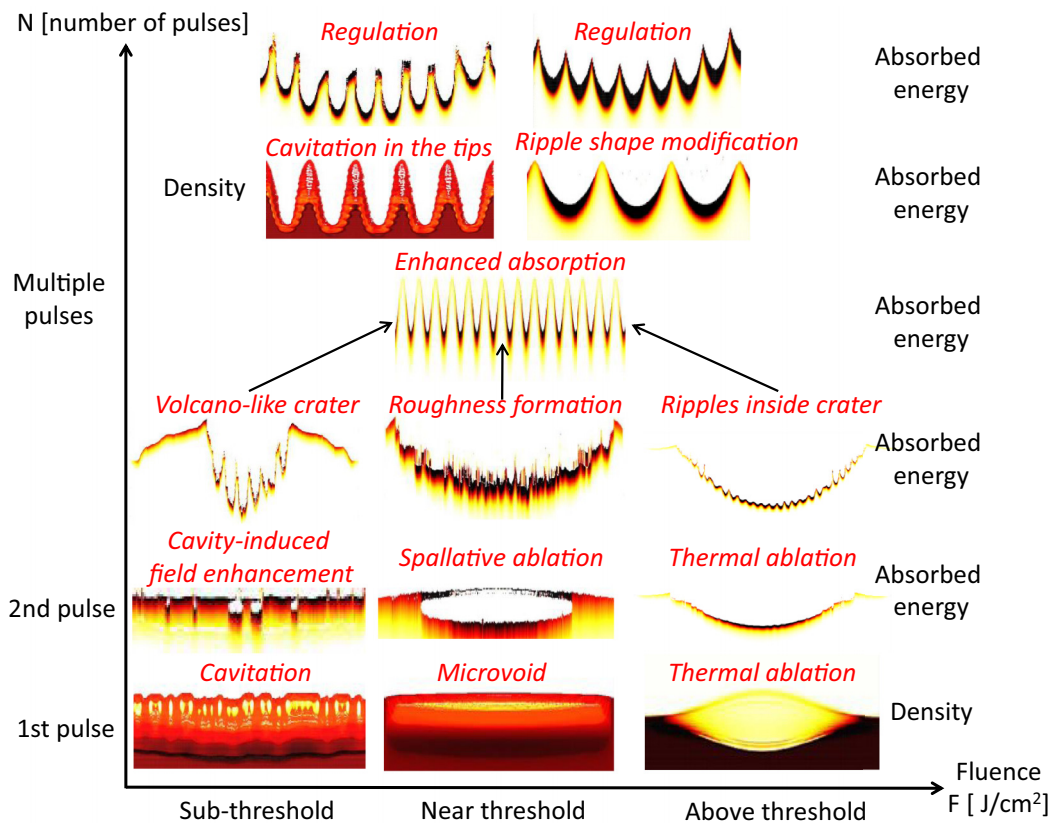


FIG. 8. Schematics of coupled electromagnetic and hydrodynamic processes upon multipulse femtosecond laser irradiation as a function of laser fluence and number of applied pulses. Absorbed energy is calculated by Maxwell equations (1) and (2), whereas density snapshots are obtained by the solution of compressible Navier-Stokes equations (4)–(6).

V. CONCLUSIONS

Multipulse evolution of the surface relief upon femtosecond laser irradiation is investigated by the multiphysical approach. The model includes Maxwell equations to calculate accurately the energy deposition, energy conservation law in the form of electron-ion heat transfer and diffusion equations, and compressible Navier-Stokes equations for momentum and mass conservation supported by the equation of state. Dynamic coupling of electromagnetic and hydrodynamic processes allows us to elucidate the role of feedback on evolving surface topographies as well as on amplification and stabilization of periodic surface structures.

Different pathways of surface topography evolution from the initially flat surface have been elucidated depending on laser fluence and the number of applied pulses. For lower subthreshold ablation fluence, the modification is characterized by swelling, material expansion above the initial surface level, and by nanocavity formation below the surface. The number of the cavities and the local field enhancement around the laser-induced cavities increase with the number of applied pulses, producing nanometric roughness on the surface. Coherent scattering on the laser-induced inhomogeneities lies in the origin of ripples, which are formed pulse by pulse and deepen for subthreshold fluences. The shape of the ripple profile is modified by cavitation and consequent local field enhancement at the tips of the nanostructures, contributing to ripple regulation.

Single-pulse irradiation by near-threshold ablation pulses results in microvoid formation below the surface. If several pulses are applied, a volcanolike crater is formed by spallation and material expansion around the crater. An increasing number of pulses leads to the formation of ripples and enhanced absorption of the metal surface. In contrast, the shape of the ripples is modified by thermal ablation, resulting in homogeneous temperature distribution along the whole surface and nanostructure regulation.

The laser irradiation regimes corresponding to fluences above the ablation threshold show clear trends of the increasing ablation depth by the thermal ablation mechanism. However, the laser ablation removal rate per laser power was shown to decrease for fluences five times higher than the ablation threshold due to the saturation of heat penetration depth per fluence.

The numerical results not only improve the fundamental understanding of laser ablation of metal targets, but also open new ways towards optimal efficient and clean ablation or fabrication of periodic and aperiodic nanostructures by multipulse irradiation.

ACKNOWLEDGMENTS

This work was supported by French ‘Programme d’investissements d’avenir’ through the IMOTEP Project operated by ADEME and the 3D-Hybrid project.

- [1] A. Kuchmizhak, O. Vitrik, Y. Kulchin, D. Storozhenko, A. Mayor, A. Mirochnik, S. Makarov, V. Milichko, S. Kudryashov, V. Zhakhovsky *et al.*, *Nanoscale* **8**, 12352 (2016).
- [2] X. Wang, A. Kuchmizhak, D. Storozhenko, S. Makarov, and S. Juodkazis, *ACS Appl. Mater. Interfaces* **10**, 1422 (2017).
- [3] A. H. A. Lutey, L. Gemini, L. Romoli, G. Lazzini, F. Fuso, M. Faucon, and R. Kling, *Sci. Rep.* **8**, 10112 (2018).
- [4] D. Hu, Y. Lu, Y. Cao, Y. Zhang, Y. Xu, W. Li, F. Gao, B. Cai, B.-O. Guan, C.-W. Qiu *et al.*, *ACS Nano* **12**, 9233 (2018).
- [5] C. Florian, E. Skoulas, D. Puerto, A. Mimidis, E. Stratakis, J. Solis, and J. Siegel, *ACS Appl. Mater. Interfaces* **10**, 36564 (2018).
- [6] J.-M. Guay, A. Calà Lesina, J. Baxter, G. Killaire, L. Ramunno, P. Berini, and A. Weck, *Adv. Opt. Mater.* **6**, 1800189 (2018).
- [7] G. D. Tsibidis, E. Skoulas, A. Papadopoulos, and E. Stratakis, *Phys. Rev. B* **94**, 081305(R) (2016).
- [8] X. Sedao, M. V. Shugaev, C. Wu, T. Douillard, C. Esnouf, C. Maurice, S. Reynaud, F. Pigeon, F. Garrelie, L. V. Zhigilei, and J.-P. Colombier, *ACS Nano* **10**, 6995 (2016).
- [9] X. Sedao, A. Abou Saleh, A. Rudenko, T. Douillard, C. Esnouf, S. Reynaud, C. Maurice, F. Pigeon, F. Garrelie, and J.-P. Colombier, *ACS Photonics* **5**, 1418 (2018).
- [10] M. V. Shugaev, I. Gnilitkiy, N. M. Bulgakova, and L. V. Zhigilei, *Phys. Rev. B* **96**, 205429 (2017).
- [11] A. Rudenko, J.-P. Colombier, S. Höhm, A. Rosenfeld, J. Krüger, J. Bonse, and T. E. Itina, *Sci. Rep.* **7**, 12306 (2017).
- [12] A. Rudenko, C. Mauchair, F. Garrelie, R. Stoian, and J.-P. Colombier, *Nanophotonics* **8**, 459 (2019).
- [13] B. Öktem, I. Pavlov, S. Ilday, H. Kalaycıoğlu, A. Rybak, S. Yavaş, M. Erdoğan, and F. Ö. Ilday, *Nat. Photonics* **7**, 897 (2013).
- [14] J.-M. Savolainen, M. S. Christensen, and P. Balling, *Phys. Rev. B* **84**, 193410 (2011).
- [15] S. V. Starikov and V. V. Pisarev, *J. Appl. Phys.* **117**, 135901 (2015).
- [16] C. Wu, M. S. Christensen, J.-M. Savolainen, P. Balling, and L. V. Zhigilei, *Phys. Rev. B* **91**, 035413 (2015).
- [17] S. I. Ashitkov, N. Inogamov, V. V. Zhakhovskii, Y. N. Emirov, M. B. Agranat, I. I. Oleinik, S. I. Anisimov, and V. E. Fortov, *JETP Lett.* **95**, 176 (2012).
- [18] V. I. Emel'yanov, D. A. Zayarniy, A. A. Ionin, I. V. Kiseleva, S. I. Kudryashov, S. V. Makarov, T. H. T. Nguyen, and A. A. Rudenko, *JETP Lett.* **99**, 518 (2014).
- [19] F. Baset, K. Popov, A. Villafranca, A. M. Alshehri, J.-M. Guay, L. Ramunno, and V. R. Bhardwaj, *Appl. Surf. Sci.* **357**, 273 (2015).
- [20] G. D. Tsibidis, M. Barberoglou, P. A. Loukakos, E. Stratakis, and C. Fotakis, *Phys. Rev. B* **86**, 115316 (2012).
- [21] A. Ben-Yakar, A. Harkin, J. Ashmore, R. L. Byer, and H. A. Stone, *J. Phys. D: Appl. Phys.* **40**, 1447 (2007).
- [22] M. E. Shaheen, J. E. Gagnon, and B. J. Fryer, *J. Appl. Phys.* **114**, 083110 (2013).
- [23] J. Lopez, G. Mincuzzi, R. Devillard, Y. Zaouter, C. Hönninger, E. Mottay, and R. Kling, *J. Laser Appl.* **27**, S28008 (2015).
- [24] J. Schille, L. Schneider, S. Kraft, L. Hartwig, and U. Loeschner, *Appl. Phys. A: Mater. Sci. Process.* **122**, 644 (2016).
- [25] E. Audouard, J. Lopez, B. Ancelot, K. Gaudfrin, R. Kling, and E. Mottay, *J. Laser Appl.* **29**, 022210 (2017).
- [26] T. Kramer, S. Remund, B. Jäggi, M. Schmid, and B. Neuenschwander, *Adv. Opt. Technol.* **7**, 129 (2018).
- [27] S. I. Anisimov and B. S. Luk'yanchuk, *Phys.-Usp.* **45**, 293 (2002).
- [28] D. Marla, U. V. Bhandarkar, and S. S. Joshi, *J. Appl. Phys.* **109**, 021101 (2011).
- [29] B. Rethfeld, D. S. Ivanov, M. E. Garcia, and S. I. Anisimov, *J. Phys. D: Appl. Phys.* **50**, 193001 (2017).
- [30] J.-P. Colombier, P. Combis, F. Bonneau, R. Le Harzic, and E. Audouard, *Phys. Rev. B* **71**, 165406 (2005).
- [31] M. E. Povarnitsyn, T. E. Itina, M. Sentis, K. V. Khishchenko, and P. R. Levashov, *Phys. Rev. B* **75**, 235414 (2007).
- [32] V. I. Mazhukin, M. G. Lobok, and B. Chichkov, *Appl. Surf. Sci.* **255**, 5112 (2009).
- [33] L. V. Zhigilei, Z. Lin, and D. S. Ivanov, *J. Phys. Chem. C* **113**, 11892 (2009).
- [34] A. Miloshevsky, M. C. Phillips, S. S. Harilal, P. Dressman, and G. Miloshevsky, *Phys. Rev. Mater.* **1**, 063602 (2017).
- [35] K.-H. Leitz, H. Koch, A. Otto, and M. Schmidt, *Appl. Phys. A: Mater. Sci. Process.* **106**, 885 (2012).
- [36] A. N. Volkov and L. V. Zhigilei, *Int. J. Heat Mass Transf.* **112**, 300 (2017).
- [37] J. Reif, O. Varlamova, S. Uhlig, S. Varlamov, and M. Bestehorn, *Appl. Phys. A: Mater. Sci. Process.* **117**, 179 (2014).
- [38] J. E. Sipe, J. F. Young, J. S. Preston, and H. M. van Driel, *Phys. Rev. B* **27**, 1141 (1983).
- [39] J. Z. P. Skolski, G. R. B. E. Römer, J. Vincenc Obona, and A. J. Huis in't Veld, *J. Appl. Phys.* **115**, 103102 (2014).
- [40] A. Rudenko, C. Mauchair, F. Garrelie, R. Stoian, and J. Colombier, *Appl. Surf. Sci.* **470**, 228 (2019).
- [41] U. S. Inan and R. A. Marshall, *Numerical Electromagnetics: The FDTD Method* (Cambridge University Press, Cambridge, UK, 2011).
- [42] E. Bévilion, J.-P. Colombier, B. Dutta, and R. Stoian, *J. Phys. Chem. C* **119**, 11438 (2015).
- [43] J. A. Roden and S. D. Gedney, *Microwave Opt. Technol. Lett.* **27**, 334 (2000).
- [44] P. B. Corkum, F. Brunel, N. K. Sherman, and T. Srinivasan-Rao, *Phys. Rev. Lett.* **61**, 2886 (1988).
- [45] A. P. Kanavin, I. V. Smetanin, V. A. Isakov, Y. V. Afanasiev, B. N. Chichkov, B. Wellegehausen, S. Nolte, C. Momma, and A. Tünnermann, *Phys. Rev. B* **57**, 14698 (1998).
- [46] I. Lomonosov, A. V. Bushman, and V. E. Fortov, in *High-Pressure Science and Technology—1993*, edited by S. C. Schmidt, J. W. Shaner, G. A. Samara, and M. Ross, AIP Conf. Proc. No. 309 (AIP, New York, 1994), pp. 117–120.
- [47] C. S. Kim, Thermophysical properties of stainless steels, Technical Report No. ANL-75-55 (Argonne National Lab., Illinois, USA, 1975), pp. 1–24.
- [48] J. J. Valencia and P. N. Quested, in *Modeling for Casting and Solidification Processing*, edited by K.-O. Yu (CRC, Boca Raton, FL, 2001), p. 189.
- [49] F. H. Harlow and A. A. Amsden, *J. Comput. Phys.* **17**, 19 (1975).
- [50] J. D. Anderson, *Computational Fluid Dynamics* (Springer, Berlin, 1992), pp. 15–51.
- [51] J. B. Freund, *AIAA J.* **35**, 740 (1997).
- [52] A. Mani, *J. Comput. Phys.* **231**, 704 (2012).
- [53] C. W. Hirt and B. D. Nichols, *J. Comput. Phys.* **39**, 201 (1981).
- [54] X. Li, F. Lu, H. Cui, X. Tang, and Y. Wu, *Int. J. Adv. Manufacturing Technol.* **72**, 241 (2014).
- [55] D. E. Grady, *J. Mech. Phys. Solids* **36**, 353 (1988).

- [56] A. Rudenko, H. Ma, V. P. Veiko, J.-P. Colombier, and T. E. Itina, *Appl. Phys. A: Mater. Sci. Process.* **124**, 63 (2018).
- [57] P. T. Mannion, J. Magee, E. Coyne, G. M. O'connor, and T. J. Glynn, *Appl. Surf. Sci.* **233**, 275 (2004).
- [58] D. Pietroy, Y. Di Maio, B. Moine, E. Baubeau, and E. Audouard, *Opt. Express* **20**, 29900 (2012).
- [59] D. J. O. Orzi, F. C. Alvira, and G. M. Bilmes, *Appl. Phys. A: Mater. Sci. Process.* **110**, 735 (2013).
- [60] R. Fang, A. Vorobyev, and C. Guo, *Light: Sci. Appl.* **6**, e16256 (2017).
- [61] F. Di Niso, C. Gaudiuso, T. Sibillano, F. P. Mezzapesa, A. Ancona, and P. M. Lugarà, *Opt. Express* **22**, 12200 (2014).
- [62] X. Sedao, M. Lenci, A. Rudenko, N. Faure, A. Pascale-Hamri, J.-P. Colombier, and C. Mauchair, *Opt. Lasers Eng.* **116**, 68 (2019).
- [63] S. Amoruso, G. Ausanio, R. Bruzzese, M. Vitiello, and X. Wang, *Phys. Rev. B* **71**, 033406 (2005).
- [64] X. Sedao, M. Lenci, A. Rudenko, A. Pascale-Hamri, J.-P. Colombier, and C. Mauchair, *Materials* **11**, 2456 (2018).
- [65] J. Bonse, J. Krüger, S. Höhm, and A. Rosenfeld, *J. Laser Appl.* **24**, 042006 (2012).
- [66] S. Razi, O. Varlamova, J. Reif, M. Bestehorn, S. Varlamov, M. Mollabashi, K. Madanipour, and M. Ratzke, *Opt. Laser Technol.* **104**, 8 (2018).
- [67] R. Le Harzic, D. Breitling, M. Weikert, S. Sommer, C. Föhl, S. Valette, C. Donnet, E. Audouard, and F. Dausinger, *Appl. Surf. Sci.* **249**, 322 (2005).
- [68] Z. Lin, L. V. Zhigilei, and V. Celli, *Phys. Rev. B* **77**, 075133 (2008).